Switchable phonon diodes using nonlinear topological Maxwell lattices

Di Zhou,[1,2,*] Jihong Ma,[3,4] Kai Sun,[1] Stefano Gonella,[3] and Xiaoming Mao[1]
[1] *Department of Physics, University of Michigan, Ann Arbor, Michigan 48109-1040, USA*
[2] *School of Physics, Georgia Institute of Technology, Atlanta, Georgia 30332, USA*
[3] *Department of Civil, Environmental, and Geo- Engineering, University of Minnesota, Minneapolis, Minnesota 55455, USA*
[4] *Center for Nanophase Materials Sciences, Oak Ridge National Laboratory, Oak Ridge, Tennessee 37831, USA*

(Received 23 December 2019; revised manuscript received 11 March 2020; accepted 12 March 2020; published 27 March 2020)

Recent progress in topological mechanics has revealed a family of Maxwell lattices that exhibit topologically protected floppy edge modes. These modes lead to a strongly asymmetric elastic wave response. In this paper, we show how topological Maxwell lattices can be used to realize nonreciprocal transmission of elastic waves. Our design leverages the asymmetry associated with the availability of topological floppy edge modes and the geometric nonlinearity built into the mechanical systems' response to achieve the desired nonreciprocal behavior, which can be further utilized to form a phonon diode via the addition of on-site pinning potentials that blocks the linear transmission and only allows the signal to transmit in one way. Finally, the nonreciprocal wave transmission can be switched on and off via topological phase transitions, paving the way to the design of cellular metamaterials that can serve as tunable topologically protected phonon diodes.

DOI: 10.1103/PhysRevB.101.104106

I. INTRODUCTION

Over the past decade, significant progress on the development of mechanical analogs of topological states of matter has fueled the new field of "topological mechanics" [1–5]. Many applications of topological mechanical metamaterials have been proposed, such as unidirectional transport using chiral edge modes [1,4,6–12], transformable topological materials [13], structures with programmed buckling or fracturing patterns [14,15], mechanical lasers [16], aperiodic topological metamaterials [17,18], geared topological metamaterials [19], and dislocation-localized softness [20].

A particularly interesting potential application of topological metamaterials is to obtain a *phonon diode*, i.e., a device that only allows sound transmission in one direction. The main requirement to achieve this goal is to break *reciprocity*. Within linear elasticity, systems with time-reversal symmetry exhibit reciprocity [21]. According to the Maxwell-Betti theorem [22–24], reciprocity implies that $u_B^{j,(1)}/F_A^i = u_A^{i,(1)}/F_B^j$, where $i, j = x, y, z$ are Cartesian components, F_A^i is the ith component of the external force exerted at input point A, and $u_B^{j,(1)}$ is the jth component of the linear elastic response probed at output point B. In the remainder of this paper, we define the quantity $\chi_{\text{out},A}^{(1)} = u_B^{j,(1)}/F_A^i$ as the linear transmission susceptibility. To achieve nonreciprocal transmission one needs to (1) break spatial-inversion symmetry and (2) either break time-reversal symmetry or include nonlinear effects. Major efforts have been devoted to the development of strategies to violate reciprocity by breaking time-reversal symmetry. For example, several active metamaterial configurations have been proposed for unidirectional edge wave propagation, such as systems of coupled gyroscopes [6,7,25,26], chiral-active fluids and plasma [27,28], dynamic phononic lattices [29], spatiotemporally modulated metamaterials [30–37], and active-liquid metamaterials [38,39].

An alternative route to break reciprocity in mechanical systems consists of leveraging the intrinsic nonlinearity of their elastic response. Recent implementations include nonlinear self-demodulation processes obtained by coupling elastically distinct layers of metamaterials [40–42], unidirectional guiding of strongly nonlinear transition waves in a bistable lattice [43], static nonreciprocal elastics [44], acoustic switching and rectification [45–47], and broadband acoustic diodes [48]. In this paper, we present an approach for nonreciprocal wave transmission in lattice systems in which the task of breaking space-inversion symmetry is accomplished through the activation of topological floppy edge modes. The nonlinear response requirements are fulfilled by the natural geometric nonlinearity of the lattice deformation, the marriage of which with the topological edge modes gives rise to large-amplitude second harmonics. The main advantage of the proposed design stems from the topological protection of the edge modes, which endows the nonreciprocal phenomena with robustness against potential defects and disorder.

Maxwell lattices are central-force lattices with average coordination number $\langle z\rangle = 2d$ (d is the spatial dimension), which puts them on the verge of mechanical instability [2,17,49,50]. They host topologically protected edge modes at zero frequency (floppy modes) which are governed by the topology of the equilibrium and compatibility matrices and therefore ultimately depend on the lattice geometry [2]. The topological edge modes lead to strongly asymmetric edge stiffness, which has been shown to result in asymmetric wave propagation characteristics, whereby certain edges allow waves to propagate into the bulk, and others localize energy at

---

[*] Corresponding author: dzhou90@gatech.edu

the boundaries [51]. Despite this asymmetry, the transmission of linear elastic waves is still reciprocal, meaning that the linear transmission susceptibilities $\chi^{(1)}_{\text{out},A}$ and $\chi^{(1)}_{\text{out},B}$ between points A and B in space are equal, in accordance with the Maxwell-Betti theorem.

To achieve nonreciprocal transmission in phonon diodes, we first localize linear excitations on lattice boundaries by driving the lattice with frequency ω in the band gap Δ. These localized modes do not propagate in space and cannot transmit elastic stress. On top of this, we propagate second harmonic bulk modes whose intensity is controlled by the amplitude of the boundary linear excitation. The generation of higher harmonics in mechanical systems with multimodal dispersive behavior and the resulting opportunities for unconventional wave manipulation and functionality enrichment in elastic metamaterials have been the subject of a number of recent studies [52–59].

In this paper we show that second harmonic modes in topological Maxwell lattices are strongly nonreciprocal, due to the contrast in stiffness between floppy and nonfloppy edges, which is a topologically protected property. Further, we demonstrate that by blocking the linear (first harmonic) modes via on-site pinning potentials (which can be realized by placing the lattice on a soft substrate), the system works as a phonon diode, in which transmission (with frequency doubled) is effectively observed in only one direction. Finally, we revisit the notion that topological kagome lattices can be reversibly transformed between different topological states with contrasting edge state landscapes through a transformation known as the "Guest mode," which involves a soft strain of the whole lattice. As a result, these lattices can be switched between strongly nonreciprocal and nearly reciprocal states through simple reversible operations.

II. NONRECIPROCITY IN A 1D TOPOLOGICAL MECHANICAL CHAIN

We start our discussion by revisiting the 1D topological mechanical chain introduced in [2], as shown in Fig. 1(a). This is the simplest lattice with topologically protected floppy edge modes that give rise to contrasting boundary rigidity. The chain consists of rigid rotors connected to fixed pivot points separated by lattice constant a. The pivot points as well as the rotors are labeled from 0 to N. The other ends of the rotors feature particles of mass m, and neighboring particles are connected with harmonic springs. The chain is subjected to open boundary conditions (OBCs) at rotors 0 and N. The equilibrium configuration is such that rotors form an angle $\bar{\theta}$ relative to the upward and downward normals. The angular displacements are denoted as $\mathbf{u} = (r\delta\theta_0, r\delta\theta_1, \dots, r\delta\theta_N)$, where $\delta\theta_n = \theta_n - \bar{\theta}$. The system consists of $N+1$ degrees of freedom and N constraints, leaving only one topological floppy mode localized on the right boundary.

Now we imagine driving the chain by a monochromatic harmonic force $F^{\text{ext}}_g(t) = Fe^{i\omega t}$ applied at the left (right) end, i.e., on rotor $g = 0$ ($g = N$), while $F^{\text{ext}}_n(t) = 0$ elsewhere. F is assumed small enough that $\delta\theta_n \ll 1$, $\forall n = 0, \dots, N$, which validates perturbation theory. We denote $\mathbf{F}^{\text{ext}}_g = (F_0, F_1, \dots, F_N)$ as the array of external forces and, as we mentioned previously, $\mathbf{F}^{\text{ext}}_0 = (F, 0, \dots, 0)$ and $\mathbf{F}^{\text{ext}}_N = (0, 0, \dots, F)$. By expanding $\mathbf{u} = \mathbf{u}^{(1)} + \mathbf{u}^{(2)} + O(F^3)$ in orders of F, we can solve for the linear elastic mode $\mathbf{u}^{(1)}$ and for second harmonic mode $\mathbf{u}^{(2)}$, respectively.

We define the input linear response function as $\chi_{\text{in}} = |u^{(1)}_{\text{in}}|/F_{\text{in}}$, where $u^{(1)}_{\text{in}}$ is the linear displacement of the rotor that is being driven. We also define $\chi^{(1)}_{\text{out}} = |u^{(1)}_{\text{out}}|/F_{\text{in}}$ ($\chi^{(2)}_{\text{out}} = |u^{(2)}_{\text{out}}|/F_{\text{in}}$), where $u^{(1)}_{\text{out}}$ ($u^{(2)}_{\text{out}}$) is the linear displacement (second harmonic displacement) at the boundary rotor opposite to the driven side.

To the linear order, Newton's equation of motion is

$$m\ddot{\mathbf{u}}^{(1)}_g = \mathbf{F}^{\text{ext}}_g - \mathbf{D}\mathbf{u}^{(1)}_g - \eta\dot{\mathbf{u}}^{(1)}_g, \tag{2.1}$$

where η is the damping coefficient, m is the particle mass, and the lower index g indicates that the force is applied at the left end if $g = 0$ (right end if $g = N$). The dynamical matrix is $\mathbf{D} = K\mathbf{C}^T\mathbf{C}$, where $\mathbf{C}_{ij} = c_1\delta_{ij} - c_2\delta_{i,j+1}$ is the compatibility matrix, and c_1, c_2 are coefficients determined by lattice geometry (see Appendix B). In the static limit, the linear elasticity is captured by the compatibility matrix $\mathbf{C}$: the floppy mode is localized on the right (left) end if $|c_1| > |c_2|$ ($|c_1| < |c_2|$). The topological protection of this floppy mode arises from the winding number of the compatibility matrix in the complex plane, and is therefore invariant against continuous deformations to the geometry of this 1D chain unless the gap closes [2]. Without losing generality, in the rest of this paper we always let $c_1 > c_2 > 0$ by allowing rotors to tilt rightward with $\bar{\theta} > 0$, so the edge floppy mode is localized on the right end of the chain. Following this convention, it is convenient to denote $\chi_{\text{in}+} = |u^{(1)}_N|/F_N$, $\chi_{\text{in}-} = |u^{(1)}_0|/F_0$ and $\chi^{(1,2)}_{\text{out}+} = |u^{(1,2)}_0|/F_N$, $\chi^{(1,2)}_{\text{out}-} = |u^{(1,2)}_N|/F_0$, where + (−) indicates that external driving is applied at the soft (rigid) end.

Above zero frequency, the dispersion relation of the bulk phonon mode reads $\omega = [(c_1 - c_2)^2 + 4c_1c_2\sin^2(\frac{1}{2}ak)]^{1/2}$, where k is the wave number. Linear elastic waves driven by external excitations with $c_1 - c_2 < \omega < c_1 + c_2$ are bulk modes. $\chi_{\text{in}+}$ and $\chi_{\text{in}-}$ are at the same order of magnitude. As ω falls below $c_1 - c_2$, linear modes localize on lattice boundaries. $\chi_{\text{in}+}/\chi_{\text{in}-}$ monotonically increases to infinity as ω approaches the static limit (see Appendix B for details). Although the stiffness differs dramatically (by orders of magnitude) on opposite boundaries, the linear elastic transmission is still reciprocal, meaning that $\chi^{(1)}_{\text{out}+} = \chi^{(1)}_{\text{out}-}$ as a manifestation of the Maxwell-Betti theorem. We verified this equality both analytically and numerically, as shown in Fig. 1(d).

Interestingly, higher-order harmonics with $\omega^{(n)} = n\omega$ that are nonlinearly generated by the edge modes are bulk modes as long as $c_1 - c_2 < \omega^{(n)} < c_1 + c_2$. In what follows, we study whether these second harmonic modes carry nonreciprocal characteristics. Newton's equation of motion for second harmonic modes is

$$m\ddot{\mathbf{u}}^{(2)}_g = \mathbf{f}^{(2)}\big(\mathbf{u}^{(1)}_g\big) - \mathbf{D}\mathbf{u}^{(2)}_g - \eta\dot{\mathbf{u}}^{(2)}_g, \tag{2.2}$$

where $\mathbf{f}^{(2)}(\mathbf{u}^{(1)}_g)$ is the second harmonic effective driving force generated by the linear displacement $\mathbf{u}^{(1)}_g$, as defined in Eq. (2.1) (see Appendix B for details). Since the effective driving is quadratic in $\mathbf{u}^{(1)}_g$, it triggers second harmonic modes with amplitude $|u^{(2)}_{\text{in}}| \propto |u^{(1)}_{\text{in}}|^2$ and frequency 2ω. External excitations with $\frac{1}{2}(c_1 - c_2) < \omega < \min(\frac{1}{2}(c_1 + c_2), c_1 - c_2)$

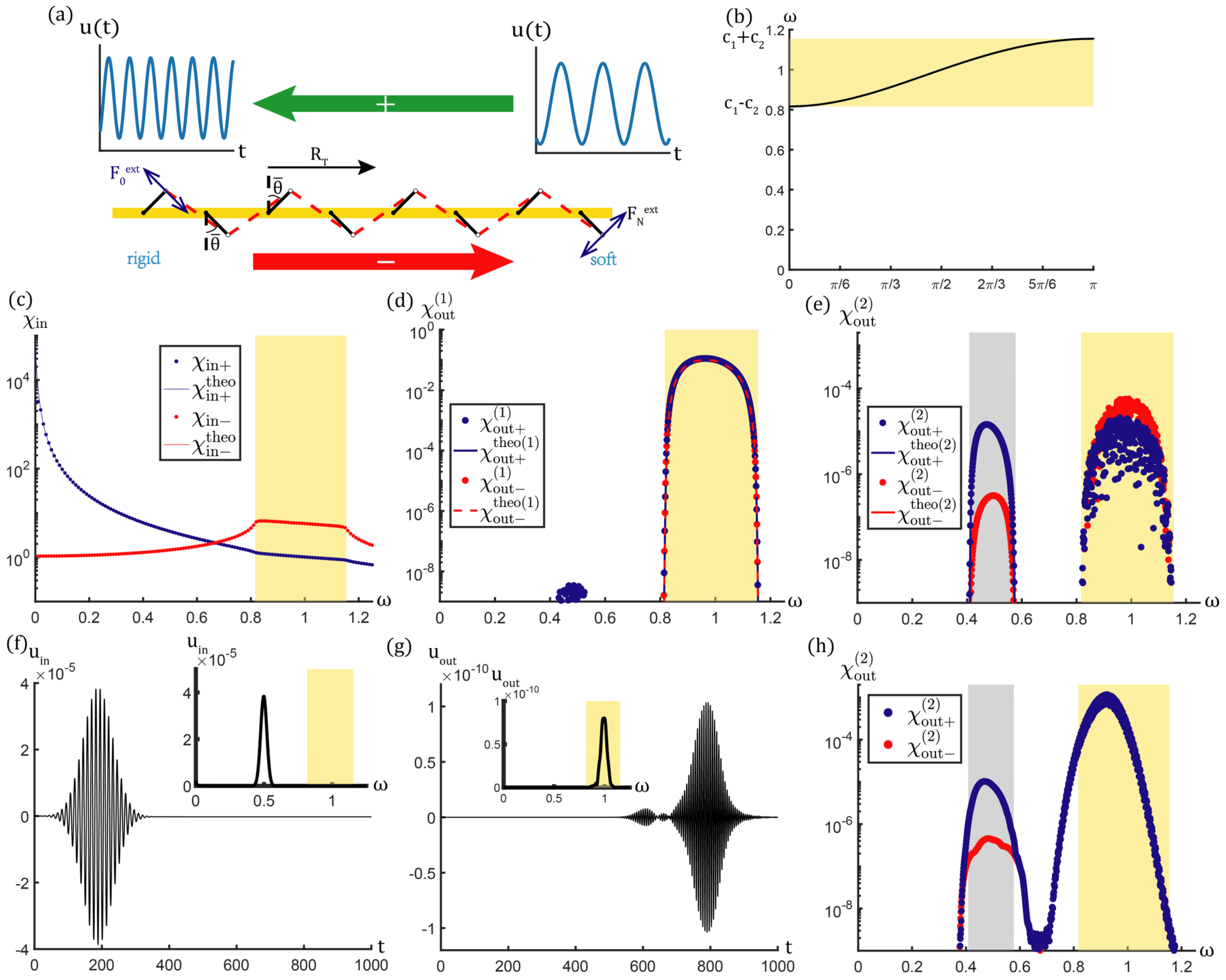

FIG. 1. Nonreciprocal wave propagation in a 1D nonlinear topological chain. (a) 1D topological mechanical chain [2] subjected to open boundary conditions with one floppy mode localized on the right edge. The "positive" ("negative") direction is marked with green (red). We apply a harmonic force $F^{\text{ext}}e^{i\omega t}$ with magnitude $F^{\text{ext}} = 10^{-5}$ and frequency $\frac{1}{2}(c_1 - c_2) < \omega = 0.5 < c_1 - c_2$ on both edges to excite linear edge modes and second harmonic bulk waves. (b) Band structure $\omega = \omega(ak)$ of the 1D chain. (c) Input-end local response function χ_{in}. We denote the bulk wave region with yellow. (d) Reciprocal transmission of linear waves with $\chi^{(1)}_{\text{out}+} = \chi^{(1)}_{\text{out}-}$. (e) Nonreciprocal transmission of second harmonic waves with $\chi^{(2)}_{\text{out}+} \gg \chi^{(2)}_{\text{out}-}$ in the frequency region $\frac{1}{2}(c_1 - c_2) < \omega < \min(\frac{1}{2}(c_1 + c_2), c_1 - c_2)$ marked in gray. We plot the output second harmonic susceptibility $\chi^{(2)}_{\text{out}}(2\omega)$ versus the input driving frequency ω. (f) Input-end response excited by a Gaussian tone burst with carrier frequency $\omega = 0.5$. (g) Output-end response featuring carrier frequency $\omega^{(2)} = 2\omega$. (h) Nonreciprocal transmission of second harmonic driven by Gaussian tone burst.

excite linear edge modes as well as second harmonic bulk waves. For a given magnitude of excitation F, the input-end linear response measured at the right edge is far greater than its counterpart measured at the left edge ($\chi_{\text{in}+} \gg \chi_{\text{in}-}$). As a result, the global wave amplitude experienced by the chain is much greater when the chain is driven from the right, leading also, in return, to significantly stronger second harmonics generation, i.e., $|\mathbf{u}^{(2)}_{g=N}| \gg |\mathbf{u}^{(2)}_{g=0}|$. Through analytical and numerical calculations we can show that $\chi^{(2)}_{\text{out}+} \gg \chi^{(2)}_{\text{out}-}$, meaning that the transmission of second harmonics is nonreciprocal, as reported in Fig. 1(e). This nonreciprocity result can be generalized to the nth harmonic mode: we obtain that $\chi^{(n)}_{\text{out}+} \gg \chi^{(n)}_{\text{out}-}$ if $\frac{1}{n}(c_1 - c_2) < \omega < \min(\frac{1}{n}(c_1 + c_2), c_1 - c_2)$. We note that besides the low-frequency regime $\omega < c_1 - c_2$, linear modes with high frequencies $\omega > c_1 + c_2$ can also localize on edges. However, they are not of interest in this paper, because the associated nonlinear harmonics are also edge excitations which cannot propagate across the lattice and therefore cannot contribute to transmission.

It is interesting to ask whether nonreciprocity still holds if the monochromatic harmonic excitation is replaced by a tone burst excitation with carrier frequency ω and Gaussian amplitude modulation, having the form $F^{\text{ext}}(t) \sim F^{\text{ext}} e^{i\omega t - (t - t_0)^2/\tau^2}$, where the parameter τ controls the spread of the Gaussian and t_0 denotes the trigger time of the packet. Since, in Fourier space, the input signal is a Gaussian function with full width at half maximum $\Delta\omega = 2\sqrt{\ln 2}/\omega\tau$, we expect that the transmission of nonlinear modes is still nonreciprocal. This conjecture is verified by numerical analysis as shown in Fig. 1(g).

It is important to note that the key ingredient to achieve nonreciprocity is the contrast in rigidity between opposite edges, and not the topological protection of the edge modes. In principle, any system with asymmetric boundary stiffness, whether this is topological or not, can realize nonreciprocity if such asymmetry is used in conjunction with nonlinear elasticity [44]. However, topologically protected floppy modes enjoy the additional attribute of being robust against disorder, noise, and stochastic damage. More interestingly, topological lattices are switchable, meaning that the topological polarization can be changed via simple, reversible operations that modify their geometry. For example, the 1D chain discussed above can be flipped to have the opposite topological polarization by propagating a soliton through the chain [60]. As we shall discuss in Sec. IV, 2D topological kagome lattices can undergo a geometric change through a soft strain of the whole lattice, called the "Guest mode" [61], to manipulate topological phases and control floppy mode localization [13] and thus boundary stiffness. Consequently, the transmission of nonlinear waves can be switched from nonreciprocal to reciprocal by reconfiguring the lattices from their topological to their nontopological form.

III. NONRECIPROCITY IN A TOPOLOGICAL KAGOME LATTICE

Having established nonreciprocity for a 1D topological chain, we now ask whether the same is true for a 2D topological lattice [2]. To this end, we consider the topological kagome lattice shown in Fig. 2(a). The lattice is ideal; i.e., it consists of point masses connected by nearest-neighbor linear springs. The unit cell contains one equilateral and one isosceles triangles, which are constructed from 6 bonds and 3 nodes marked by A, B, and C. The side length of the equilateral triangle and the longer edge of the isosceles triangle are l_0, while the shorter edge is $l_0/\sqrt{3}$. The twist angle of the isosceles triangle is 5° counterclockwise, which makes the longer edge of the isosceles triangle inclined by 5° relative to the bottom edge of the equilateral triangle [marked $\overline{AB}$ in Fig. 2(a)]. $\vec{a}_1$ and $\vec{a}_2$ are the lattice primitive vectors. The lattice, spanning the area $|N_1\vec{a}_1 \times (N_2-1)\vec{a}_2|$ in real space, is composed of $N_1 \times (N_2-1)$ unit cells and an additional layer of C sites at the bottom edge of the lattice to complete the

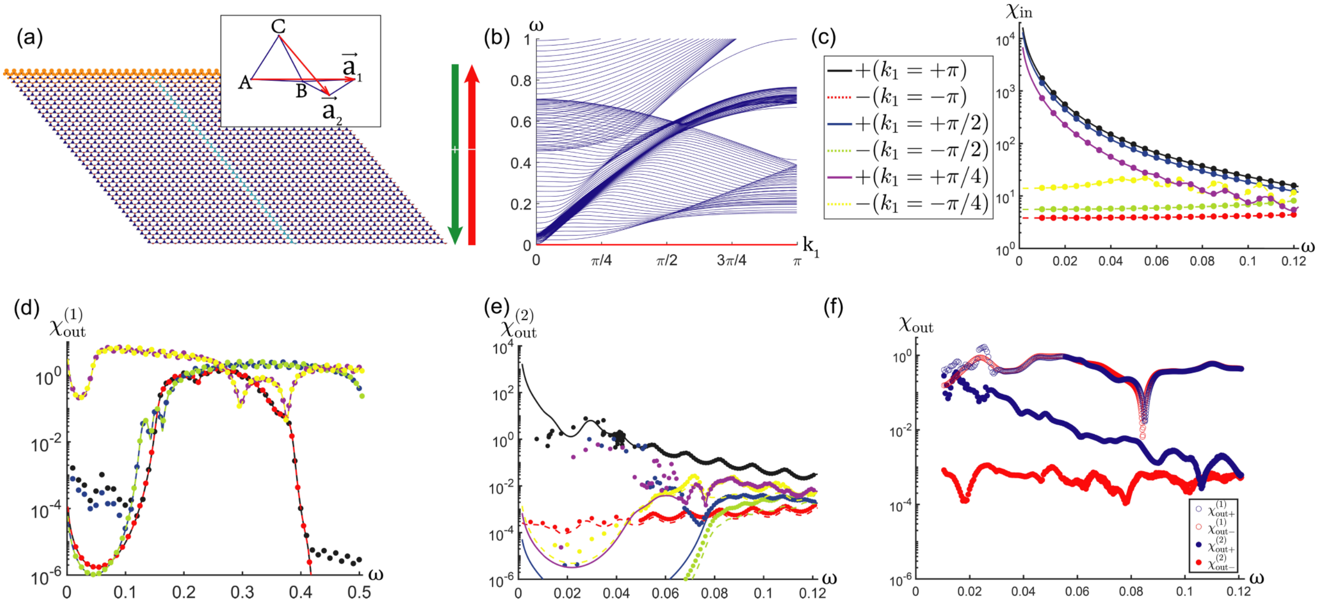

FIG. 2. Nonreciprocal wave propagation in a 2D nonlinear topological kagome lattice. (a) Topological kagome lattice, with unit cell shown in the inset, where A, B, and C label the sites and $(\vec{a}_1, \vec{a}_2)$ are the primitive vectors. The floppy modes are localized on the top boundary. Total floppy mode amplitude on each site is shown by the size of the orange disks on the site. The lattice consists of $40 \times (40-1)$ unit cells and an additional layer of 40 C sites at the bottom boundary. The lattice is subjected to periodic boundary conditions in $\vec{a}_1$ and open boundary conditions on the top and bottom sides. The supercell strip used in our analysis is marked with cyan. (b) Supercell band structure, where $k_1 = \vec{k} \cdot \vec{a}_1$. The dispersion branch of topological floppy modes is marked with red. In (c), (d), (e), and (f) we employ both analytic calculations (curves) and Newtonian mechanics simulations (dots) to measure the input local response function $\chi_{\rm in}$ and the output linear (second harmonic) susceptibilities $\chi^{(1)}_{\rm out}$ ($\chi^{(2)}_{\rm out}$). (c) Strongly asymmetric edge response function $\chi_{\rm in}(\omega, k_1)$ with $\chi_{\rm in+}(\omega, k_1) \gg \chi_{\rm in-}(\omega, -k_1)$ for waves below the bulk band ($\omega \lesssim 0.06$). The lattice is driven by a monochromatic excitation force which is spatially periodic in $\vec{a}_1$, with the wave number k_1 for the top boundary ($-k_1$ for the bottom). (d) Reciprocal transmission curves of linear elastic waves with $\chi^{(1)}_{\rm out+}(k_1) = \chi^{(1)}_{\rm out-}(-k_1)$, where the external driving force amplitude $F^{\rm ext} = 10^{-8}$. (e) Nonreciprocal transmission curves of second harmonic waves with $\chi^{(2)}_{\rm out+}(2\omega, 2k_1) \gg \chi^{(2)}_{\rm out-}(2\omega, -2k_1)$, where the external force amplitude $F^{\rm ext} = 10^{-4}$. It is worth of emphasizing that for $\omega \lesssim 0.04$, the one-way transmission of second harmonics is comparable to that of linear elastic modes in (d). (f) Nonreciprocal transmission of linear and second harmonic modes with monochromatic point driving force. The transmission of second harmonic waves is less nonreciprocal compared to (e) since the point shaking force has all k_1 wave number components. The first harmonic modes are bulk modes since long-wavelength components are in the band.

triangles. It is subjected to periodic boundary condition in $\vec{a}_1$ and open boundary conditions at the top and bottom edges.

We start by introducing a *supercell* analysis of this lattice. For convenience we denote $k_1 = \vec{k} \cdot \vec{a}_1$ and $k_2 = \vec{k} \cdot \vec{a}_2$ as the wave numbers along the primitive vectors. We further decompose the lattice in supercell strips directed along $\vec{a}_2$, as marked in cyan in Fig. 2(a), and we apply Bloch's conditions along $\vec{a}_1$. Within a supercell, the unit cells are labeled from 1 to $N_2 - 1$ going from top to bottom, and the C sites on the bottom layer are labeled as N_2. The internal nodal displacements of unit cell n_2 (with $1 \leqslant n_2 \leqslant N_2 - 1$) are denoted as $\mathbf{u}_{n_2} = (u^x_{n_2A}, u^y_{n_2A}, u^x_{n_2B}, u^y_{n_2B}, u^x_{n_2C}, u^y_{n_2C})$. The displacement field of the supercell strip is therefore denoted as $\mathbf{u} = (\mathbf{u}_1, \mathbf{u}_2, \dots, \mathbf{u}_{N_2})$. The lattice is driven by a monochromatic harmonic force acting vertically and with amplitude varying periodically in the $\vec{a}_1$ direction, i.e., $\vec{F}^{\text{ext}}_{n_1,g}(t) = e^{i\omega t - ik_1 n_1}\vec{F}_C$ with $\vec{F}_C = (0, F)$ at the top boundary (bottom boundary) of C sites labeled by $g = 1$ ($g = N_2$) and $\vec{F}^{\text{ext}}_{n_1,n_2}(t) = 0$ otherwise. F is assumed to be small such that all $|\vec{u}_{n_1n_2,A}|$, $|\vec{u}_{n_1n_2,B}|$, and $|\vec{u}_{n_1n_2,C}| \ll l_0$, validating perturbation theory. By expanding $\mathbf{u} = \mathbf{u}^{(1)} + \mathbf{u}^{(2)} + O(F^3)$, we can solve Newton's equation of motion for the linear mode $\mathbf{u}^{(1)}$ and for second harmonic mode $\mathbf{u}^{(2)}$, as detailed in Appendix C.

The analysis of wave propagation in the 2D lattice follows the steps used for the 1D chain, albeit with the additional wave number k_1 describing spatial variation in the horizontal direction (with periodic boundary conditions). Specifically, the dynamical matrix of this supercell strip is $\mathbf{D} = K\mathbf{C}^{\dagger}(k_1)\mathbf{C}(k_1)$. $\mathbf{C}(k_1)$ is the compatibility matrix given by $\mathbf{C}_{ij}(k_1) = \mathbf{C}_1(k_1)\delta_{ij} + \mathbf{C}_2(k_1)\delta_{i+1,j}$, where $\mathbf{C}_1(k_1)$ and $\mathbf{C}_2(k_1)$ are intracell and intercell compatibility matrices, respectively (see Appendix C for details). To the linear order of displacement, Newton's equation of motion is the same as Eq. (2.1), where η and m are damping coefficient and particle mass, respectively, and g indicates that the input force is applied at the layer of C sites indexed $g = 1$ at the top (layer of C sites indexed $g = N_2$ at the bottom) of the lattice. The static system is characterized by the *polarization vector* $\vec{R}_T$, which is a topological invariant. Mechanical lattices with a well-defined polarization exhibit topological floppy edge modes exponentially localized at the boundary toward which $\vec{R}_T$ points. The configuration of Fig. 2(a) has a polarization vector $\vec{R}_T = \vec{a}_1 - \vec{a}_2$. The floppy modes are therefore localized on the top edge, making this edge much softer than the bottom one. We use lower index + (−) to indicate that the external signal is applied where the floppy modes are localized (opposite to the floppy mode localization). It is therefore convenient to denote $\chi_{\text{in}+} = |u^{y,(1)}_1|/F^y_1$ and $\chi_{\text{in}-} = |u^{y,(1)}_{N_2}|/F^y_{N_2}$ as the soft edge and rigid edge linear response functions, respectively. Similarly, we denote $\chi^{(1)}_{\text{out}+} = |u^{y,(1)}_{N_2}|/F^y_1$ ($\chi^{(2)}_{\text{out}+} = |\vec{u}^{(2)}_{N_2}|/F^y_1$) and $\chi^{(1)}_{\text{out}-} = |u^{y,(1)}_{N_2}|/F^y_1$ ($\chi^{(2)}_{\text{out}-} = |\vec{u}^{(2)}_{N_2}|/F^y_1$) as the linear (second harmonic) transmission susceptibilities driven by external forces applied at the soft and rigid boundaries, respectively.

Linear wave propagation is governed by the supercell band structure which stems from the eigenvalue problem $\det(\mathbf{D} - m\omega^2\mathbf{I}) = 0$. The band structure is gapped except for the trivial translational zero mode point at $k_1 = 0$. Given the wave number k_1 of the applied force, the linear response is a bulk mode if $\omega > \Delta(k_1)$, where $\Delta(k_1)$ is the lowest bulk eigenvalue in the band structure, and $\chi_{\text{in}+}$ and $\chi_{\text{in}-}$ are of the same order of magnitude. As ω falls below $\Delta(k_1)$, linear modes localize on the soft boundary of the lattice. $\chi_{\text{in}+}/\chi_{\text{in}-}$ monotonically increases to infinity as ω approaches zero. Despite the contrasting boundary stiffness at low frequencies, the linear elastic transmission is still reciprocal, i.e., $\chi^{(1)}_{\text{out}+}(k_1) = \chi^{(1)}_{\text{out}-}(-k_1)$, similar to what we obtained for the 1D topological chain. We validate this equality through analytical and numerical calculations, as shown in Fig. 2(d).

While linear modes can localize on the lattice boundaries, nonlinearly generated components with $(\omega^{(n)}, k^{(n)}_1) = (n\omega, nk_1)$ can be bulk waves as long as $\omega^{(n)} > \Delta(k^{(n)}_1)$. The equation of motion for the second harmonic mode is given by Eq. (2.2). External excitations with frequency $\frac{1}{2}\Delta(2k_1) < \omega < \Delta(k_1)$ generate linear boundary modes and second harmonic bulk waves. Moreover, given the same magnitude F of external force, the input-end frequency response function of the floppy edge is far greater than that of the hard edge ($\chi_{\text{in}+} \gg \chi_{\text{in}-}$), which renders second harmonic bulk modes excited at the floppy edge much greater than those excited at the hard edge, i.e., $|\mathbf{u}^{(2)}_{g=N_2}| \gg |\mathbf{u}^{(2)}_{g=1}|$. The transmission of second harmonics is therefore strongly nonreciprocal, with $\chi^{(2)}_{\text{out}+} \gg \chi^{(2)}_{\text{out}-}$, which is verified numerically as shown in Fig. 2(e). We note that because of the strong localized linear excitations for small frequencies $\omega \lesssim 0.04$ [Fig. 2(c)], this asymmetric transmission of second harmonic modes could be as great as the linear reciprocal transmission [Fig. 2(d)]. This conclusion can be generalized to the nonreciprocal transmission of the nth harmonic mode with $\chi^{(n)}_{\text{out}+} \gg \chi^{(n)}_{\text{out}-}$ if $\frac{1}{n}\Delta(nk_1) < \omega < \Delta(k_1)$.

While, so far, the analysis has followed almost *verbatim* the same steps of the 1D problem, one important difference is that the 2D lattice phonon band depends on k_1 (the wave number in the horizontal direction imposed along the boundary). Thus, the width of the gap Δ and the resulting availability of nonreciprocal propagation depend on the choice of k_1. In particular, the lattice always has translational zero modes since $\lim_{k_1 \to 0} \Delta(k_1) \to 0$. As a result, if we drive the system with a point force applied at a given location on the boundary (which ostensibly excites all values of k_1), we are bound to observe weaker signatures of nonreciprocity. In other words, the differences in behavior observed by exciting the soft and hard edges will be vastly reduced, as the long-wavelength components of the excited linear waves are in both cases bulk modes that do not display asymmetry. Moreover, despite the strong nonreciprocity, this kagome lattice cannot be, strictly speaking, defined as a proper phonon diode. This is because the linear mode, which is reciprocal and always transmitted both ways, is much stronger than the second harmonic mode and always dominates the total response, completely overshadowing any asymmetry in the nonlinear response. In order to mitigate the aforementioned issues, in the next section we propose an evolution of the lattice design meant to work as a proper phonon diode for all wave numbers.

IV. NONRECIPROCITY IN A KAGOME LATTICE WITH AN ON-SITE POTENTIAL

We consider a modification of the topological kagome lattice discussed in Sec. III, where a weak on-site pinning potential is added to every mass point i, with $V_i = \frac{1}{2}K'\vec{u}_i^2$ and $K' \ll K$. This operation, which practically elastically connects each site to a fixed ground point, can be thought of as the equivalent model of placing the lattice on a soft substrate (or soft elastic foundation). It penalizes particles from moving away from their rest positions, and therefore eliminates the lattice trivial translational zero modes. Since the weak pinning rigidly shifts the band up by $\Delta' = \sqrt{K'/m}$, now the signals with frequency below Δ' will excite edge modes. The weak pinning does not change the landscape of asymmetric boundary stiffness of the lattice, meaning that $\chi_{\text{in}+} \gg \chi_{\text{in}-}$ still holds as long as $\omega < \Delta'$. Thus, linear edge modes are still preferentially localized on the soft boundary.

The fundamental consequence of having a full low-frequency gap is that, as long as $\frac{1}{2}\Delta' < \omega < \Delta'$, an external excitation that is periodic along the boundary will excite linear edge modes and second harmonic bulk modes for any arbitrary wave number k_1. Consequently, the nonreciprocal behavior will be observed in the response to a point excitation prescribed at a given location on the boundary, thus eliminating the limitation of the previous configuration. As shown in Fig. 3(d), the second harmonic positive transmission is indeed stronger than the linear transmission for a point excitation. We

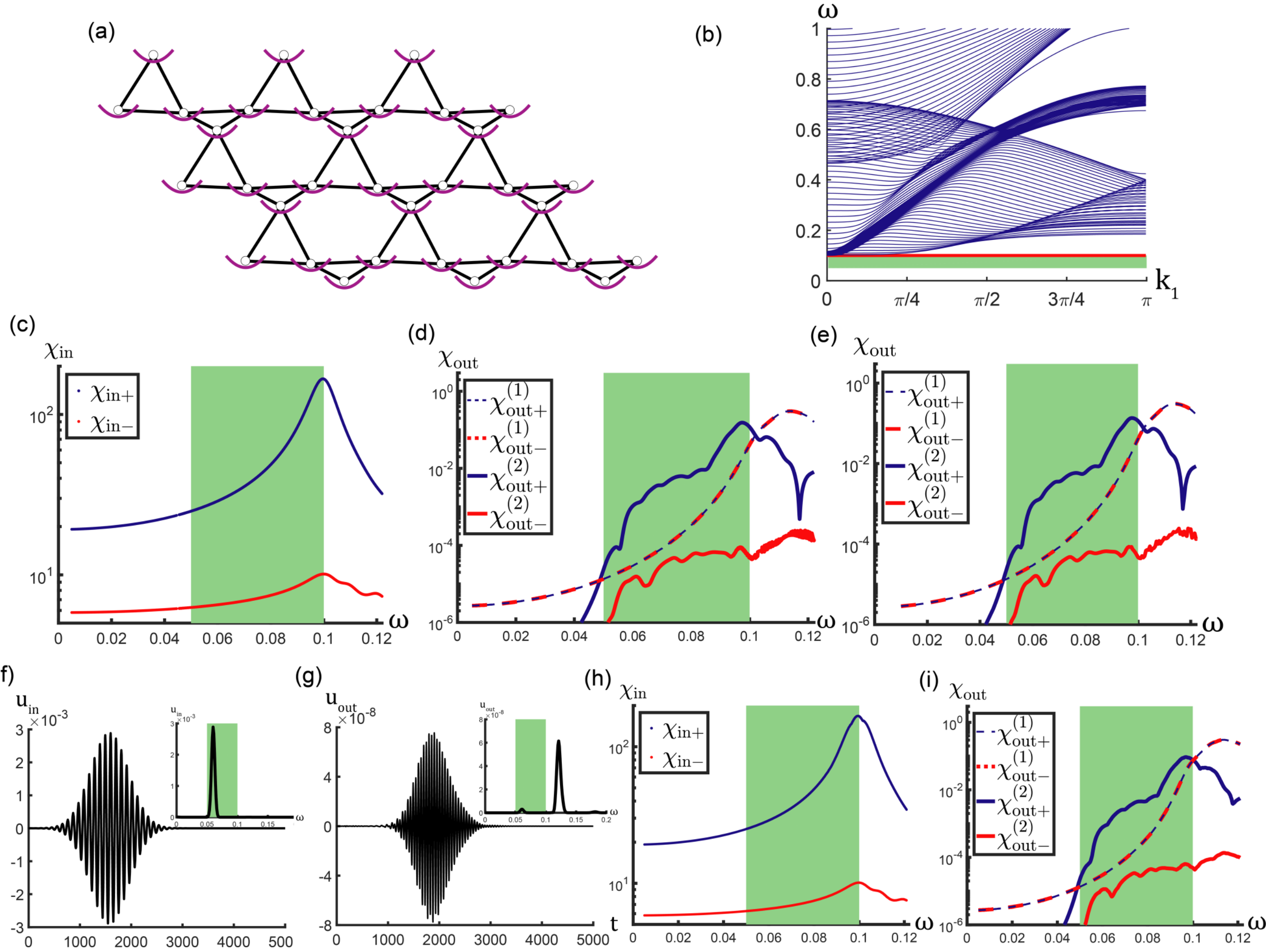

FIG. 3. One-way propagation of second harmonic waves in a topological kagome lattice with on-site pinning potentials. (a) Schematic illustration of the lattice with on-site potential. (b) Band structure of supercell strip with on-site potential $K' = K/100$, which fully gapped the spectrum at low frequency. We mark the edge mode excitation with red at $\omega = \sqrt{K'/m}$, and the frequency range where second harmonics 2ω are in the band with green. In (c), (d), (e), (h), and (i) we employ Newtonian mechanics simulations to measure the input local response function χ_{in} and the output susceptibility χ_{out} against point shaking force at an arbitrary C site on top or bottom. (c) Asymmetric stiffness of the boundary at which the point harmonic excitation is applied (with force amplitude $F^{\text{ext}} = 10^{-4}$). (d) Nonreciprocal transmission of second harmonic modes. The transmission susceptibility in the positive direction (i.e., transmission from soft edge to hard edge), marked in blue, is much larger than that in the negative direction marked in red, and also much larger than the first harmonics (dashed lines). (e) Nonreciprocal transmission of second harmonic modes calculated including bending stiffness $\kappa = 10^{-5}K$. (f) Input-end displacement time history for monochromatic point excitation in the form of Gaussian tone burst (frequency spectrum in the inset). (g) Output-end displacement time history for tone burst excitation where the frequency is twice the input wave frequency. (h) Input-end frequency response for tone burst excitation. (i) Output linear and second harmonic transmission susceptibilities for tone burst excitation. The result is very similar to panel (d), confirming the robustness of the results in transitioning from steady-state to transient regimes of excitation.

can conclude that the topological lattice with pinning potential is now a well-defined phonon diode.

These results still hold when finite bending stiffness at the hinges is included [51]. In Fig. 3(e) our numerical results indeed show that when bending stiffness is introduced by adding the contribution of next-nearest-neighbor interactions, the nonreciprocal transmission is still significant. Finally, the results also hold for a Gaussian tone burst excitation $F^{\text{ext}}(t) \sim F^{\text{ext}} e^{i\omega t-(t-t_0)^2/\tau^2}$. The numerical analysis results reported in Fig. 3(i) show that the transmission is still nonreciprocal, similarly to the result of the 1D topological mechanical chain.

V. LATTICE RECONFIGURATION AND NONRECIPROCITY SWITCHING

An interesting feature of Maxwell lattices with spring-mass interactions is that they can undergo uniform soft deformations, in which all the unit cells are twisted in the same fashion while leaving the bond lengths unstretched. Such uniform deformation, known as the "Guest mode," can manipulate the geometrical parameters that control the topological phase of the kagome lattice and, consequently, its polarization and the rigidity established on opposite boundaries [13]. Starting from the unit cell configuration in Fig. 2(a), by uniformly rotating all the isosceles triangles counterclockwise by 30° relative to the hinges on the equilateral triangles, the lattice enters a nontopological phase, as shown in Fig. 4(a). The total number of floppy modes remains the same, but, instead of being all localized on the top edge, they localize on both lattice boundaries with nearly comparable stiffness.

The discussion of reconfiguration above applies directly to the case where there is no substrate. It is clear that by reconfiguration, the second harmonics transmission changes by orders of magnitude, whereas the linear transmission is always open. Similarly to what has been discussed in Sec. IV, the substrate can be used to open a gap and block the linear transmission, making the system a true diode. In order to allow the substrate and the reconfiguration to be realized in the same system, we have the following two proposals. First, by preparing a double-layered lattice in which the top and bottom layers work as the kagome lattice and the substrate, respectively, we can reconfigure both layers together. We fix the bottom substrate while letting the top lattice capable of propagating waves serve as the acoustic diode. The second design is to place the kagome lattice on a continuous board. The kagome lattice can be detached and reattached to the soft board for lattice reconfiguration.

Consequently, given an external force excitation with amplitude F and frequency $\frac{1}{2}\Delta' < \omega < \Delta'$, the transmission of any nonlinearly generated second harmonics is reciprocal, because the linear modes driven from opposite lattice boundaries, which are ultimately responsible for second harmonic generation, have the same order of magnitude. In conclusion, through uniform soft twisting modes that allow reversible reconfiguration between topological and nontopological phases, Maxwell lattices have the ability to switch between reciprocal and nonreciprocal transmission regimes of nonlinear elastic

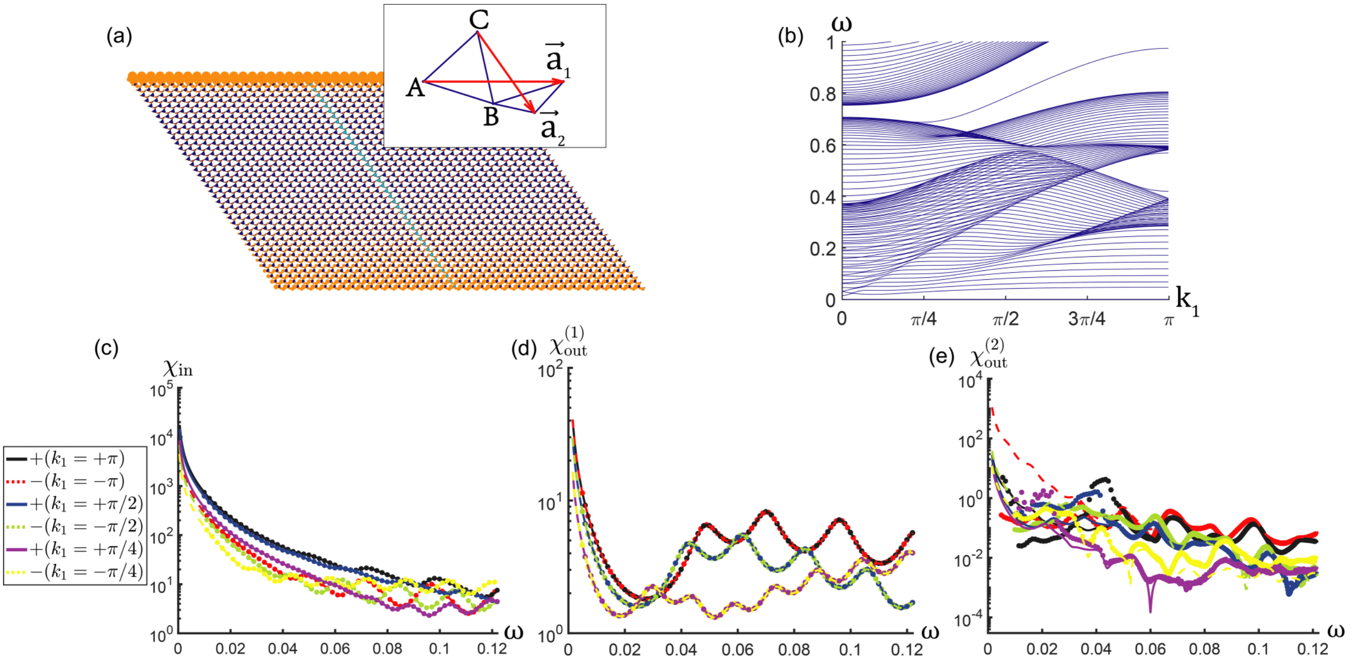

FIG. 4. Near-reciprocal wave propagation in nontopological kagome lattice, which is related to the topological kagome lattice by a soft-strain reconfiguration. (a) Kagome lattice in the nontopological regime. The floppy mode amplitudes shown by the size of the orange disks on each site are localized on both the top and the bottom boundaries. (b) Supercell band structure of nontopological kagome lattice. (c) Different from the topological kagome lattice, the edge response functions $\chi_{\text{in}}(\omega, k_1)$ are significantly more symmetric between top and bottom boundaries. We drive the lattice with spatially periodic harmonic force with wave numbers $k_1 = +\pi, +\pi/2, +\pi/4$ on top boundary ($k_1 = -\pi, -\pi/2, -\pi/4$ on bottom). (e) Almost reciprocal transmission of second harmonic waves with various wave numbers (force amplitude $F^{\text{ext}} = 10^{-4}$). The second harmonic transmission $\chi^{(2)}_{\text{out}+}(2\omega, 2k_1)$ is always comparable to $\chi^{(2)}_{\text{out}-}(2\omega, -2k_1)$.

waves without the need to physically disassemble and reassemble the system.

VI. DISCUSSION AND CONCLUDING REMARKS

In this paper we have studied the connection between the nonreciprocity and topology in Maxwell lattices. Here, the conditions required for the establishment of nonreciprocal behavior come from the interplay between two factors: on one hand, the availability of floppy edge modes, which yield large boundary deformations and trigger a nonlinear response; on the other hand, the topological polarization, which guarantees asymmetry across the lattice.

Differently from the previous work by Coulais *et al.* [44], who studied static nonreciprocal elasticity in both topological and nontopological quasi-1-dimensional (1D) mechanical metamaterials, our design focuses on nonzero frequencies. The concept is developed first using a 1D topological mechanical chain and subsequently generalized to 2D topological kagome lattices [2], paving the way to applications in realistic mechanical metamaterials. The foundational argument of the proposed concept is that topological floppy edge modes produce contrasting stiffness on opposite lattice boundaries. We find that signals with frequency $\omega < \Delta$, where Δ is the onset of a (partial or total) band gap, excite edge modes. These modes localize asymmetrically, leading to larger deformation that promotes second harmonic generation at the floppy edge. Second harmonic contributions are bulk modes if $\omega > \frac{1}{2}\Delta$, and, in these conditions, they can propagate through the medium. Finally, because of the asymmetry mentioned above, such transmission is highly nonreciprocal. Interestingly, this second harmonic transmission could be as large as linear transmission since the amplitudes of second harmonics $A^{(2)} \propto A^2$ grow faster than linear amplitudes.

By adding an on-site pinning potential to every particle, the band structure of the topological kagome lattice is shifted up by Δ'. In these conditions, external signals with $\frac{1}{2}\Delta' < \omega < \Delta'$ excite linear modes that remain localized at the edges and second harmonic bulk modes that propagate across the lattice. Hence, the second harmonic positive transmission is greater than the fundamental mode transmission and is therefore not trivially overshadowed by the linear response. With this improved configuration, this effect is found to be true for any external harmonic excitation applied at the edges, regardless of the wave number established along the boundary. Consequently, the result also holds for point excitations, which represent realistic conditions in practice. We have concluded that the lattice with on-site pinning potential fulfills all the requirements to be labeled a phonon diode. In addition, one can control the geometry of the Maxwell lattice through a Guest mode to switch between topological and nontopological phases. This lattice reconfiguration allows us to manipulate reciprocal and nonreciprocal transmission of elastic waves without disassembling or reassembling the structure.

The idea of nonlinear bulk waves driven by linear edge modes is not limited to second harmonics. One can observe nth-order harmonic bulk modes at the output end as long as the input frequency satisfies the condition $\frac{1}{n}\Delta < \omega < \frac{1}{n-1}\Delta$ ($n \geqslant 2$), while all lower-order harmonics are localized on the boundaries and cannot propagate. A methodological problem to be considered in performing such an extension is associated with the intrinsic limitations of perturbation theory. Since the amplitude of the output signal becomes exponentially small when the order increases, i.e., $A^{(n)} \sim A^n$, higher-order harmonic bulk modes become progressively more difficult to be observed. It would thus be interesting to study these phenomena in regimes of strong nonlinearity which invalidate perturbation theory. This kind of study would likely present new challenges arising from the interplay between topological states of matter and nonlinear chaos dynamical theory.

It is worth exploring experimental realization of the proposed nonlinear phonon diode. In a recent experiment [51], Ma *et al.* studied the specimen of topological kagome lattice manufactured via a water jet cutting from a sheet of acrylonitrile butadiene styrene. The ideal hinges that appear in the theoretical models are replaced by ligaments capable of supporting bending deformation, which is ubiquitous in realistic physical structures. This experimental system provides a natural setup to test our theory.

Finally, our investigation so far has been limited to 1D and 2D topological Maxwell lattices. An analogous study of nonreciprocal transmission in 3D topological lattices appears to be possible as a natural extension within the proposed framework. This would open the doors to a broader range of engineering applications and will be one of the next directions in our research.

ACKNOWLEDGMENT

This work was supported by the National Science Foundation (Grant No. NSF-EFRI-1741618).

APPENDIX A: RECIPROCITY OF LINEAR ELASTIC SYSTEMS WITH TIME-REVERSAL SYMMETRY

With time-reversal symmetry, the transmission of linear elastic modes is reciprocal, meaning that the transmission susceptibilities from point A to point B and from point B to point A are equal. This is the essence of the Maxwell-Betti theorem [22–24]. In this section we verify this theorem by considering a d-dimensional general lattice based on spring-mass interactions. Within linear elasticity, Newton's equation of motion is

$$m\ddot{\vec{u}}_n = -\eta\dot{\vec{u}}_n - \vec{\nabla}_n V + \vec{F}_n^{\text{ext}}(t), \tag{A1}$$

where n denotes a lattice site, η is the damping coefficient, V is the lattice potential energy, $\vec{\nabla}_n = \sum_{i=1}^d \hat{e}_i \partial_{u_n^{(i)}}$, and $\vec{F}_n^{\text{ext}}$ is the external driving force. We rewrite the displacement field as an Nd-dimensional vector $\mathbf{u} = (\vec{u}_1, \vec{u}_2, \dots, \vec{u}_N)$ and rewrite the external driving as an Nd-dimensional vector $\mathbf{F}^{\text{ext}}$. The linear elastic mode can be calculated as

$$\mathbf{u}(\omega) = \mathbf{G}(\omega)\mathbf{F}^{\text{ext}}(\omega), \tag{A2}$$

where $\mathbf{G}(\omega) = [\mathbf{D} + (-m\omega^2 + i\eta\omega)\mathbf{I}]^{-1}$ is the frequency response function, and $\mathbf{D}$ is the dynamical matrix. By using an orthogonal transformation $\mathbf{S}$ that relates u_n to the normal modes u_α through $u_\alpha = \sum_n S_{\alpha n} u_n$, we can express the normal modes as follows,

$$u_\alpha(\omega) = G_\alpha F_\alpha^{\text{ext}}(\omega), \tag{A3}$$

where $G_\alpha(\omega) = [\epsilon_\alpha + (-m\omega^2 + i\eta\omega)]^{-1}$, and ϵ_α is the αth eigenvalue of the dynamical matrix $\mathbf{D}$. We plug in the driving force at point A to calculate the displacement at B, with $u_B(\omega) = \sum_\alpha S_{\alpha B} G_\alpha(\omega) S_{\alpha A} F_A^{\text{ext}}(\omega)$. Similarly, we plug in the driving force at B to calculate displacement at A with $u_A(\omega) = \sum_\alpha S_{\alpha A} G_\alpha(\omega) S_{\alpha B} F_B^{\text{ext}}(\omega)$. It is evident that $u_A(\omega)/F_B^{\text{ext}}(\omega) = u_B(\omega)/F_A^{\text{ext}}(\omega)$, meaning that the transmission of linear modes is reciprocal in real space in any elastic system with time-reversal symmetry.

APPENDIX B: ANALYTICAL CALCULATION OF LINEAR AND SECOND HARMONIC MODES IN A 1D TOPOLOGICAL MECHANICAL CHAIN

As shown in Fig. 1(a), the 1D topological mechanical chain consists of rigid bars of length r, free to rotate about hinges separated by the distance a, creating repeated 2-site unit cell of length $2a$. A mass point m is attached to the end of each bar, and the neighboring ends are connected by harmonic springs with spring constant K. The equilibrium configuration is such that each rotor makes an angle $\bar{\theta}$ relative to the upward or downward normals. The angular displacement of rotor n is $u_n = r\delta\theta_n$. We label the rotors from 0 to N, with open boundary conditions at rotors 0 and N. We apply an external angular driving along the tangential direction of rotor g with $F_n^{\text{ext}}(t) = Fe^{i\omega t}\delta_{ng}$. F is not large, making angular displacements of all rotors $u_n \ll r$, which further validates perturbation theory. It is convenient to rewrite the external force as $F \to \lambda F$, where $\lambda \ll 1$. The full Newton equation of motion is

$$m\ddot{u}_{n,g} = (\vec{T}_{n-1} - \vec{T}_n)\cdot\hat{t}_n + F_n^{\text{ext}} - \eta\dot{u}_{n,g}, \tag{B1}$$

where the lower index g indicates that the elastic mode is in response to the external driving at rotor g. The open boundary conditions at rotor 0 and rotor N are given by

$$\vec{T}_{-1} = \vec{T}_N = 0, \tag{B2}$$

where $\vec{T}_n = T_n\hat{n}_n$ is the tension in bond n connecting sites n and $n+1$. $\hat{n}_n$ is the unit vector of bond n, and $\hat{t}_n$ is the tangential unit vector of rotor n. We expand the tangential component of bond tension in orders of u_n/r, denoted by $(\vec{T}_{n-1} - \vec{T}_n)\cdot\hat{t}_n = f_n^{(1)} + f_n^{(2)} + O(u^3)$. The leading order is

$$f_n^{(1)} = m[c_1c_2(u_{n+1} + u_{n-1}) - (c_1^2 + c_2^2)u_n], \tag{B3}$$

with

$$c_{1,2} = \sqrt{\frac{K}{m}\frac{(a \pm 2r\sin\bar{\theta})\cos\bar{\theta}}{\sqrt{a^2 + 4r^2\cos^2\bar{\theta}}}}, \tag{B4}$$

where $\bar{\theta} > 0$ is assumed in this paper, leading to $c_1 > c_2$. The second-order term is

$$\begin{aligned} f_n^{(2)}(u_n) = {} & mr^{-1}\big(C_1u_{n-1}^2 + C_2u_{n-1}u_n + C_3u_n^2\big) \\ & + mr^{-1}\big(C_4u_{n+1}^2 + C_5u_{n+1}u_n + C_6u_n^2\big), \end{aligned} \tag{B5}$$

with $C_{1,2,3,4,5,6}$ being constants determined by the geometric parameters of the chain. In our calculations, we choose $a = 2r$ and $\theta = \pi/4$. The coefficients are given by

$$\begin{aligned} 2C_1 &= C_5 = \frac{K}{4m}(-1 + \sqrt{2}), \\ 2C_4 &= C_2 = \frac{K}{4m}(-1 - \sqrt{2}), \\ C_3 &= \frac{K}{24m}(5 - \sqrt{2}), \quad C_6 = \frac{K}{24m}(5 + \sqrt{2}). \end{aligned} \tag{B6}$$

We denote $\mathbf{u} = (u_0, u_1, \ldots, u_N)$ as the angular displacement of the particles, and expand it in orders of λ, with $\mathbf{u} = \mathbf{u}^{(1)} + \mathbf{u}^{(2)} + O(\lambda^3)$, where $\mathbf{u}^{(1)}$ and $\mathbf{u}^{(2)}$ are linear and second harmonic modes, respectively. We further denote $\mathbf{F}^{\text{ext}} = (\lambda F, 0, \ldots, 0)^T$ [$\mathbf{F}^{\text{ext}} = (0, 0, \ldots, \lambda F)$] as the external driving force driven at rotor $g = 0$ ($g = N$), and denote $\mathbf{f}^{(2)}(\mathbf{u}^{(1)}) = (f_0^{(2)}, f_1^{(2)}, \ldots, f_N^{(2)})$ as the second harmonic effective feedback force generated by the linear elastic modes. By expanding Eq. (B1) up to the second order of λ, one obtains

$$\begin{aligned} m\ddot{\mathbf{u}}_g^{(1)} + m\ddot{\mathbf{u}}_g^{(2)} + O(\lambda^3) = {} & \big(\mathbf{F}^{\text{ext}} - \mathbf{D}\mathbf{u}_g^{(1)} - \eta\dot{\mathbf{u}}_g^{(1)}\big) \\ & + \big[\mathbf{f}_g^{(2)}\big(\mathbf{u}_g^{(1)}\big) - \mathbf{D}\mathbf{u}_g^{(2)} - \eta\dot{\mathbf{u}}_g^{(2)}\big] + O(\lambda^3), \end{aligned} \tag{B7}$$

where $\mathbf{D} = K[(c_1^2 + c_2^2)\delta_{ij} - c_1c_2(\delta_{i,j+1} + \delta_{i,j-1})]$ is the dynamical matrix. By matching the equations of motion in orders of λ, we solve for the linear mode

$$\mathbf{u}_g^{(1)}(\omega) = \mathbf{G}(\omega)\mathbf{F}^{\text{ext}}(\omega), \tag{B8}$$

and for the second harmonic mode

$$\mathbf{u}_g^{(2)}(2\omega) = \mathbf{G}(2\omega)\mathbf{f}_g^{(2)}\big(\mathbf{u}_g^{(1)}\big), \tag{B9}$$

subjected to the open boundary conditions at rotors 0 and N. The frequency response function of the 1D chain is

$$\mathbf{G}(\omega) = [\mathbf{D} + (-m\omega^2 + i\eta\omega)\mathbf{I}]^{-1}. \tag{B10}$$

The dispersion relation of the only bulk phonon mode is $\omega(k) = [(c_1 - c_2)^2 + 4c_1c_2\sin^2(ak/2)]^{1/2}$, where k is the wave number. The band has lower limit $\Delta = |c_1 - c_2|$ and upper limit $\Delta' = |c_1 + c_2|$. Thus, the linear mode is a bulk mode if $\Delta < \omega < \Delta'$, while it is an edge mode if $\omega < \Delta$. According to Eq. (B8), the generic solution for a linear mode is

$$\begin{aligned} u_{n,g}^{(1)} &= a_g\lambda_1^n + A_g\lambda_2^n, \quad 0 \leqslant n \leqslant g, \\ u_{n,g}^{(1)} &= b_g\lambda_1^n + B_g\lambda_2^n, \quad g \leqslant n \leqslant N, \end{aligned} \tag{B11}$$

where $\lambda_{1,2}$ are given by

$$\lambda_{1,2} = \tfrac{1}{2}\big(-\gamma \pm \sqrt{\gamma^2 - 4}\big), \tag{B12}$$

with $\gamma = \frac{\omega^2}{c_1c_2} - \frac{c_1}{c_2} - \frac{c_2}{c_1} - \frac{i\eta\omega}{c_1c_2}$. Through Eq. (B8) and Eq. (B11) we can solve for a_g, A_g, b_g, B_g. We let $g = 0$ and $g = N$ to obtain the linear modes when the external driving is applied at rotors 0 and N. Given the definition of the local response function, $\chi_{\text{in}}(\omega) = |u_{\text{in}}^{(1)}(\omega)|/F_{\text{in}}(\omega)$, at rotor 0 (rigid end, $\chi_{\text{in}-}$) and rotor N (soft end, $\chi_{\text{in}+}$), the local response functions are given by

$$\begin{aligned} \chi_{\text{in}+}(\omega) &= (mc_1|c_1 - c_2\lambda_1|)^{-1}, \\ \chi_{\text{in}-}(\omega) &= (mc_2|c_2 - c_1\lambda_1|)^{-1}, \end{aligned} \tag{B13}$$

where we have used $\lim_{N\to\infty}|\lambda_2/\lambda_1|^N = 0$ when $\omega < c_1 - c_2$. The ratio $\chi_{\text{in}+}/\chi_{\text{in}-}$ tells which end of the 1D chain has greater displacement in response to external loading. In the limit of $\eta \to 0$, analytical calculations reveal that

$$\begin{aligned} \chi_{\text{in}+}/\chi_{\text{in}-} &> 1, & \omega &< \omega^*, \\ \chi_{\text{in}+}/\chi_{\text{in}-} &< 1, & \omega^* &< \omega < c_1 - c_2, \end{aligned} \tag{B14}$$

where $\omega^* = (c_1^2 - c_2^2)/\sqrt{2(c_1^2 + c_2^2)}$. As long as $\omega < \omega^*$, the response linear edge mode of the right end is greater than that of the left side. The linear transmission susceptibility, defined by $\chi^{(1)}_{\text{out}}(\omega) = |u^{(1)}_{\text{out}}(\omega)|/F(\omega)$, is given by

$$\chi^{(1)}_{\text{out}-}(\omega) = \chi^{(1)}_{\text{out}+}(\omega) = \frac{1}{m}\frac{\lambda_1^{-N-1}(\lambda_2 - \lambda_1)}{\omega^2 - i\eta\omega}. \tag{B15}$$

The fact that the linear transmission susceptibilities are equal is a testament to the reciprocity of linear waves.

We further study the second harmonic modes based on Eq. (B9). To calculate the second harmonic mode displacement $\mathbf{u}^{(2)}_g$, we notice that $\mathbf{u}^{(2)}_g = \sum_{g'=0}^{N}\mathbf{u}^{(2)}_{g'g}$, where $\mathbf{u}^{(2)}_{g'g}$ is the displacement field of the chain in response to external force $f^{(2)}_{g'g}$ applied at a single rotor g'. The displacement field is given by

$$\mathbf{u}^{(2)}_{g'g}(2\omega) = \mathbf{G}(2\omega)\mathbf{f}^{(2)}_{g'g}(2\omega), \tag{B16}$$

where we denote the external driving at rotor g' as an $N \times 1$ vector $\mathbf{f}^{(2)}_{g'g} = (0, 0, \dots, f^{(2)}_{g'g}, \dots, 0)$. The generic solution of Eq. (B16) is of the following form,

$$\begin{aligned} u^{(2)}_{n,g'g} &= c_{g'g}\mu_1^n + C_{g'g}\mu_2^n, & 0 &\leqslant n \leqslant g', \\ u^{(2)}_{n,g'g} &= d_{g'g}\mu_1^n + D_{g'g}\mu_2^n, & g' &\leqslant n \leqslant N, \end{aligned} \tag{B17}$$

where $\mu_{1,2}$ satisfy

$$\mu_{1,2} = \tfrac{1}{2}(-\nu \pm \sqrt{\nu^2 - 4}), \tag{B18}$$

with $\nu = \frac{4\omega^2}{c_1c_2} - \frac{c_1}{c_2} - \frac{c_2}{c_1} - \frac{2i\eta\omega}{c_1c_2}$. Through Eq. (B16) and Eq. (B17) we solve for $c_{g'g}, C_{g'g}, d_{g'g}, D_{g'g}$ to determine $\mathbf{u}^{(2)}_{g'g}(2\omega)$. Finally, given the definition of second harmonic transmission susceptibility, $\chi^{(2)}_{\text{out}} = |u^{(2)}_{\text{out}}(2\omega)|/F(\omega)$, we obtain

$$\begin{aligned} \chi^{(2)}_{\text{out}+} &= \frac{1}{F}\sum_{g'=0}^{N}(c_{g',g=N} + C_{g',g=N}), \\ \chi^{(2)}_{\text{out}-} &= \frac{1}{F}\sum_{g'=0}^{N}\big(\mu_1^N d_{g',g=0} + \mu_2^N D_{g',g=0}\big). \end{aligned} \tag{B19}$$

The second harmonic transmission susceptibility is determined by $\mathbf{f}^{(2)}_{g'g}$, which in turn is proportional to the square of the linear elastic wave amplitude. This consideration is essential in explaining how the asymmetric local response function $\chi^{(1)}_{\text{in}+} \gg \chi^{(1)}_{\text{in}-}$ results in the nonreciprocal transmission of second harmonic modes ($\chi^{(2)}_{\text{out}+} \gg \chi^{(2)}_{\text{out}-}$).

APPENDIX C: ANALYTICAL CALCULATION OF LINEAR AND SECOND HARMONIC MODES IN A 2D TOPOLOGICAL KAGOME LATTICE

In this section we calculate linear and second harmonic modes in a 2D topological kagome lattice. The unit cell is shown in Fig. 2(a) and consists of 6 bonds, with rest lengths l_i and unit vector directions $\hat{n}_i = (\cos\theta_i, \sin\theta_i)$, $i = 1, 2, \dots, 6$. We define the 2×2 "dynamical matrix" of bond i as

$$\mathbf{D}_i = K\hat{n}_i\hat{n}_i, \quad i = 1, 2, \dots, 6. \tag{C1}$$

$\vec{a}_1$ and $\vec{a}_2$ are primitive vectors. The lattice has the periodic boundary condition in $\vec{a}_1$ and the open boundary condition in $\vec{a}_2$, leaving the top and bottom boundaries open.

The compatibility matrix of the quasi-1D strip of the deformed kagome lattice is $\mathbf{C}_{ij}(k_1) = \mathbf{C}_1(k_1)\delta_{ij} + \mathbf{C}_2(k_1)\delta_{i+1,j}$, where $\mathbf{C}_1(k_1)$ and $\mathbf{C}_2(k_1)$ are intracell and intercell compatibility matrices, respectively:

$$\mathbf{C}_1 = \begin{pmatrix} \cos\theta_1 & \sin\theta_1 & -\cos\theta_1 & -\sin\theta_1 & 0 & 0 \\ 0 & 0 & \cos\theta_2 & \sin\theta_2 & -\cos\theta_2 & -\sin\theta_2 \\ -\cos\theta_3 & -\sin\theta_3 & 0 & 0 & \cos\theta_3 & \sin\theta_3 \\ -e^{ik_1}\cos\theta_4 & -e^{ik_1}\sin\theta_4 & 0 & 0 & 0 & 0 \\ e^{ik_1}\cos\theta_5 & e^{ik_1}\sin\theta_5 & -\cos\theta_5 & -\sin\theta_5 & 0 & 0 \\ 0 & 0 & \cos\theta_6 & \sin\theta_6 & 0 & 0 \end{pmatrix},$$

$$\mathbf{C}_2 = \begin{pmatrix} 0 & 0 & 0 & 0 & 0 & 0 \\ 0 & 0 & 0 & 0 & 0 & 0 \\ 0 & 0 & 0 & 0 & 0 & 0 \\ 0 & 0 & 0 & 0 & \cos\theta_4 & \sin\theta_4 \\ 0 & 0 & 0 & 0 & 0 & 0 \\ 0 & 0 & 0 & 0 & -\cos\theta_6 & -\sin\theta_6 \end{pmatrix}. \tag{C2}$$

We simplify the lattice to a quasi-1D strip by applying the Bloch condition along $\vec{a}_1$ to obtain a finite supercell strip with N_2 unit cells. Thus, the elastic wave $\mathbf{u}_{n_1n_2} = e^{ik_1n_1}\mathbf{u}_{n_2}$, with $k_1 = \vec{k}\cdot\vec{a}_1$. We denote the displacement of cell n_2 as $\mathbf{u}_{n_2} = (u^x_{n_2A}, u^y_{n_2A}, u^x_{n_2B}, u^y_{n_2B}, u^x_{n_2C}, u^y_{n_2C})$, and further denote the displacement of the entire strip as $\mathbf{u} = (\mathbf{u}_1, \mathbf{u}_2, \dots, \mathbf{u}_{N_2})$. To fully gap the band structure of the lattice, we introduce an on-site potential $\frac{1}{2}K'\mathbf{u}\mathbf{u}^T$ by embedding the lattice on a soft substrate.

Before calculating the elastic waves, we first derive the tension of a bond connecting two sites i and j. The bond rest length is l_0 and its unit vector is $\hat{n} = (\cos\theta, \sin\theta)$. We denote the relative displacement of the bond as $\Delta\vec{u}_{ij} = \vec{u}_j -$

$\vec{u}_i$, and expand the tension in orders of it, with $\vec{T}_i = \vec{F}_i + \vec{f}_i + O(\Delta u_{ij}^3)$. The leading-order term is

$$\vec{F}_i = K(\hat{n}\hat{n})\Delta\vec{u}_{ij} \tag{C3}$$

and the second-order ones are

$$\begin{aligned} f_i^x = \frac{K}{4l_0}\big\{&6\cos\theta\sin^2\theta\big(\Delta u_{ij}^x\big)^2 \\ &-[3\sin(3\theta)-\sin\theta]\Delta u_{ij}^x\Delta u_{ij}^y \\ &-2\cos\theta(3\sin^2\theta-1)\big(\Delta u_{ij}^y\big)^2\big\}, \end{aligned} \tag{C4}$$

$$\begin{aligned} f_i^y = \frac{K}{4l_0}\big\{&6\sin\theta\cos^2\theta\big(\Delta u_{ij}^y\big)^2 \\ &+[3\cos(3\theta)+\cos\theta]\Delta u_{ij}^x\Delta u_{ij}^y \\ &-2\sin\theta(3\cos^2\theta-1)\big(\Delta u_{ij}^x\big)^2\big\}. \end{aligned} \tag{C5}$$

Equations (C4) and (C5) are useful to derive the effective second harmonic feedback force.

We now apply an external driving at cell g of the strip, denoted as $F_{n_1 n_2}^{\text{ext}}(t) = e^{i\omega t - ik_1 n_1}F_C^y\delta_{n_2 g}$. Thus, we further denote the external force as a $6N_2$-dimensional vector $\mathbf{F}_g^{\text{ext}} = (\mathbf{F}_1^{\text{ext}}, \mathbf{F}_2^{\text{ext}}, \ldots, \mathbf{F}_{N_2}^{\text{ext}})$. We assume F_C^y is not too large, rendering all displacements $|\vec{u}_{A,B,C}| \ll l_{i=1,2,\ldots,6}$, which further validates perturbation theory. Thus, we expand $\mathbf{u}$ in orders of F_C^y, as $\mathbf{u} = \mathbf{u}^{(1)} + \mathbf{u}^{(2)} + O(F^3)$, where $\mathbf{u}^{(1)}$ and $\mathbf{u}^{(2)}$ are linear and second harmonic modes. We define the frequency response function as

$$\mathbf{G}(\omega, k_1) = [\mathbf{D}(k_1) + (-m\omega^2 + K' + i\eta\omega)\mathbf{I}]^{-1}, \tag{C6}$$

where $\mathbf{D}(k_1) = K\mathbf{C}^\dagger(k_1)\mathbf{C}(k_1)$ is the dynamical matrix of the supercell strip. Thus, the linear mode is

$$\mathbf{u}_g^{(1)}(\omega, k_1) = \mathbf{G}(\omega, k_1)\mathbf{F}^{\text{ext}}(\omega, k_1). \tag{C7}$$

The second harmonic mode is

$$\mathbf{u}_g^{(2)}(2\omega, 2k_1) = \mathbf{G}(2\omega, 2k_1)\mathbf{f}^{(2)}(\mathbf{u}_g^{(1)}), \tag{C8}$$

where $\mathbf{f}^{(2)}(\mathbf{u}_g^{(1)}) = (\mathbf{f}_1, \mathbf{f}_2, \ldots, \mathbf{f}_{N_2})$ is the second harmonic effective feedback force generated by the linear mode $\mathbf{u}_g^{(1)}$, as shown in Eqs. (C4) and (C5).

The generic form of linear mode $\mathbf{u}_g^{(1)}$ is given as follows:

$$\begin{aligned} \mathbf{u}_{n_2,g}^{(1)} &= \sum_{\alpha=1}^{4} a_{g\alpha}\lambda_\alpha^{n_2}\boldsymbol{\phi}_\alpha, \quad 1 \leqslant n_2 \leqslant g, \\ \mathbf{u}_{n_2,g}^{(1)} &= \sum_{\alpha=1}^{4} b_{g\alpha}\lambda_\alpha^{n_2}\boldsymbol{\phi}_\alpha, \quad g+1 \leqslant n_2 \leqslant N_2, \end{aligned} \tag{C9}$$

where λ_α, $\alpha = 1, 2, 3, 4$ are the eigenvalues of $[\mathbf{D}(k_1, \lambda) + (-m\omega^2 + K' + i\eta\omega)\mathbf{I}]$, and $\boldsymbol{\phi}_\alpha$ are the corresponding 6×1 eigenvectors. $\mathbf{D}(k_1, \lambda)$ is the following 6×6 matrix,

$$\mathbf{D}(k_1, \lambda) = \begin{pmatrix} \mathbf{D}_1 + \mathbf{D}_3 + \mathbf{D}_4 + \mathbf{D}_5 & -\mathbf{D}_1 - e^{-ik_1}\mathbf{D}_5 & -\mathbf{D}_3 - \lambda e^{-ik_1}\mathbf{D}_4 \\ -\mathbf{D}_1 - e^{ik_1}\mathbf{D}_5 & \mathbf{D}_1 + \mathbf{D}_2 + \mathbf{D}_5 + \mathbf{D}_6 & -\mathbf{D}_2 - \lambda\mathbf{D}_6 \\ -\mathbf{D}_3 - \lambda^{-1}e^{ik_1}\mathbf{D}_4 & -\mathbf{D}_2 - \lambda^{-1}\mathbf{D}_6 & \mathbf{D}_2 + \mathbf{D}_3 + \mathbf{D}_4 + \mathbf{D}_6 \end{pmatrix}. \tag{C10}$$

$a_{g\alpha}$ and $b_{g\alpha}$, $\alpha = 1, 2, 3, 4$, are constants determined by the open boundary condition at cell 1,

$$(\mathbf{D}_4 e^{ik_1}, \mathbf{D}_6, -\mathbf{D}_4 - \mathbf{D}_6) \cdot \big(u_{0,gA}^{(1)x}, u_{0,gA}^{(1)y}, u_{0,gB}^{(1)x}, u_{0,gB}^{(1)y}, u_{1,gC}^{(1)x}, u_{1,gC}^{(1)y}\big)^T = 0, \tag{C11}$$

and the open boundary condition at cell N_2,

$$(\mathbf{D}_3, \mathbf{D}_2, -\mathbf{D}_2 - \mathbf{D}_3)\mathbf{u}_{N_2,g}^{(1)} = 0. \tag{C12}$$

Together with Eq. (C7), we solve $a_{g\alpha}$ and $b_{g\alpha}$ to obtain the linear mode $\mathbf{u}_g^{(1)}$.

We then calculate the second harmonic mode based on Eq. (C8). However, it is not easy to solve $\mathbf{u}_g^{(2)}$, because the effective second harmonic feedback force, $\mathbf{f}_g^{(2)}(2\omega, 2k_1)$, is applied at every cell. In order to simplify this problem, we consider the mode $\mathbf{u}_{g'g}^{(2)}(2\omega, 2k_1)$ in response to the second harmonic effective feedback force $\mathbf{f}_{g'g}^{(2)}$ applied at a single cell g',

$$\mathbf{u}_{g'g}^{(2)}(2\omega, 2k_1) = \mathbf{G}(2\omega, 2k_1)\mathbf{f}_{g'g}^{(2)}(2\omega, 2k_1). \tag{C13}$$

The generic form of $\mathbf{u}_{g'g}^{(2)}(2\omega, 2k_1)$ is given by

$$\begin{aligned} \mathbf{u}_{n_2,g'g}^{(2)} &= \sum_{\beta=1}^{4} c_{g'g\beta}\mu_\beta^{n_2}\boldsymbol{\varphi}_\beta, \quad 1 \leqslant n_2 \leqslant g', \\ \mathbf{u}_{n_2,g'g}^{(2)} &= \sum_{\beta=1}^{4} d_{g'g\beta}\mu_\beta^{n_2}\boldsymbol{\varphi}_\beta, \quad g'+1 \leqslant n_2 \leqslant N_2, \end{aligned} \tag{C14}$$

where μ_β, $\beta = 1, 2, 3, 4$, are the eigenvalues of $[\mathbf{D}(2k_1, \mu) + (-4m\omega^2 + K' + 2i\eta\omega)\mathbf{I}]$, and $\boldsymbol{\varphi}_\beta$ are the corresponding 6×1 eigenvectors. $c_{g'g\beta}$ and $d_{g'g\beta}$ are constants determined by the boundary condition at cell 1,

$$\begin{aligned} &(\mathbf{D}_4 e^{ik_1}, \mathbf{D}_6, -\mathbf{D}_4 - \mathbf{D}_6) \cdot \\ &\quad \big(u_{0,g'gA}^{(2)x}, u_{0,g'gA}^{(2)y}, u_{0,g'gB}^{(2)x}, u_{0,g'gB}^{(2)y}, u_{1,g'gC}^{(2)x}, u_{1,g'gC}^{(2)y}\big)^T = 0, \end{aligned} \tag{C15}$$

and the open boundary condition at cell N_2,

$$(\mathbf{D}_3, \mathbf{D}_2, -\mathbf{D}_2 - \mathbf{D}_3)\mathbf{u}_{N,g'g}^{(2)} = 0. \tag{C16}$$

Together with Eq. (C13), we solve $c_{g'g\beta}$ and $d_{g'g\beta}$ to obtain $\mathbf{u}_{g'g}^{(2)}$. Finally, the second harmonic displacement is $\mathbf{u}_g^{(2)} = \sum_{g'=1}^{N_2}\mathbf{u}_{g'g}^{(2)}$.

APPENDIX D: NUMERICAL SIMULATION OF THE INPUT LOCAL RESPONSE FUNCTION AND OUTPUT TRANSMISSION SUSCEPTIBILITY

1. Numerical details of the 1D topological mechanical chain

We perform Newtonian mechanics simulations to study the nonreciprocal transmission in a 1D topological mechanical chain. In the numerics, the chain is composed of $N = 100$ rotor particles (i.e., it is composed of $N/2 = 50$ diatomic unit cells) and is subjected to OBCs at rotors $N = 0$ and $N = 99$ [Fig. 1(a)]. We set the particle mass $m = 1$, the spring constant $K = 1$, and the damping coefficient $\eta = 0.01$. The equilibrium configuration of the particles is that they make an angle $\bar{\theta} = \pi/4$ to the upward and downward normals. The particles can rotate about fixed hinges with the radii $r = 1$, and the nearest-neighbor hinges are separated by the distance $a = 2$. Hence the springs connecting nearest-neighbor particles make an angle $\arctan(2r\cos\bar{\theta}/a) = 35.3^\circ$ to the horizontal line. Consequently, in this geometric configuration, $c_1 = 0.986$, $c_2 = 0.169$ [c_1, c_2 are defined in Eq. (B4)], and the band gap is $\Delta = c_1 - c_2 = 0.817$ [Fig. 1(b)]. We apply a monochromatic angular shaking force $F^{\text{ext}}(t) = F^{\text{ext}}e^{i\omega t}$ at rotor $N = 99$ (the floppy boundary) and at rotor $N = 0$ (the rigid boundary), with the magnitude $F^{\text{ext}} = 10^{-5}$ and the frequency $\omega = 0.5$, $\frac{1}{2}\Delta < \omega < \Delta$, to illustrate the excitation of linear edge modes and second harmonic bulk waves. In order to confirm the establishment of the steady-state conditions, we wait $1000 \times (2\pi/\omega)$ before we make any displacement measurements. We further plot the linear response function $\chi_{\text{in}\pm}(\omega)$ in Fig. 1(c), linear transmission susceptibility $\chi^{(1)}_{\text{out}\pm}(\omega)$ in Fig. 1(d), and second harmonic transmission susceptibility $\chi^{(2)}_{\text{out}\pm}(\omega)$ in Fig. 1(e) by varying the driving frequency from $\omega = 0.01$ to $\omega = 1.25$. Finally, we replace the harmonic excitation with a Gaussian tone burst $F^{\text{ext}}(t) \sim F^{\text{ext}}e^{i\omega t-(t-t_0)^2/\tau^2}$ and ask whether the nonreciprocity still holds. By driving the lattice with the Gaussian tone burst with carrier frequency $\omega = 0.5$, force amplitude $F^{\text{ext}} = 10^{-5}$, and the spread parameter $\tau = 10\pi/\omega$, we illustrate the input response displacement in Fig. 1(f) and the second harmonic transmission signal in Fig. 1(g). We plot the second harmonic transmission susceptibility curve in Fig. 1(h) to verify nonreciprocal transmission against Gaussian tone burst by varying the driving force frequency from $\omega = 0.01$ to $\omega = 1.25$ ($\tau = 10\pi/\omega$ varies accordingly).

2. Numerical details of the 2D generalized kagome lattice

In the simulation, a finite topological kagome lattice which spans $N_1\vec{a}_1 \times (N_2 - 1)\vec{a}_2$ area in real space ($N_1 = N_2 = 40$) is considered. The lattice is made of $40 \times (40 - 1)$ unit cells with an additional layer of C sites at the bottom. We connect the leftmost particles to the rightmost ones with harmonic springs to provide the periodic boundary condition in the $\vec{a}_1$ direction, and we leave the C sites of top and bottom boundaries free to realize open boundary conditions. By applying a vertical harmonic force $\vec{F}^{\text{ext}} = (0, F^{\text{ext}})$ either on the top edge or bottom edge C sites, we drive the lattice and we compute the displacement of mass points using a Newtonian dynamics scheme with damping. Here we set the particle mass $m = 1$, the spring constant $K = 1$, the damping coefficient $\eta = 0.01$, and the side length of the equilateral triangle $l_0 = 1$. We let the force amplitude $F^{\text{ext}} = 10^{-8}$ to measure the reciprocal transmission of linear waves, and we let the force amplitude $F^{\text{ext}} = 10^{-4}$ when measuring the nonreciprocal transmission of second harmonics. We vary the driving frequency from $\omega = 0.0055$ to $\omega = 0.1210$ to plot the input response function $\chi_{\text{in}}(\omega, k_1)$ in Fig. 2(c), linear transmission susceptibility $\chi^{(1)}_{\text{out}}(\omega, k_1)$ in Fig. 2(d), second harmonic transmission susceptibility $\chi^{(2)}_{\text{out}}(2\omega, 2k_1)$ in Fig. 2(e), and second harmonic transmission susceptibility $\chi^{(2)}_{\text{out}}(2\omega)$ against point shaking force in Fig. 2(f). In order to make sure steady-state conditions are established, we wait $400 \times (2\pi/\omega)$ before we make any displacement reading. We collect displacements $\vec{u}_{1C}(t)$ and $\vec{u}_{N_2C}(t)$ on the two edges. By applying fast Fourier transformation, we convert displacement time histories into their frequency spectra, $\vec{u}_{1C}(\omega)$ and $\vec{u}_{N_2C}(\omega)$. The elastic response is obtained via summation of multiple modes,

$$\vec{u}_{n_2C}(\omega) = \vec{u}^{(1)}_{n_2C}(\omega) + \vec{u}^{(2)}_{n_2C}(2\omega) + \cdots, \tag{D1}$$

where $\vec{u}^{(1)}_{n_2C}(\omega) = (u^{x,(1)}_{n_2C}(\omega), u^{y,(1)}_{n_2C}(\omega))$ and $\vec{u}^{(2)}_{n_2C}(2\omega) = (u^{x,(2)}_{n_2C}(2\omega), u^{y,(2)}_{n_2C}(2\omega))$. $u^{x,(1)}_{n_2C}(\omega)$, $u^{y,(1)}_{n_2C}(\omega)$, $u^{x,(2)}_{n_2C}(2\omega)$, and $u^{y,(2)}_{n_2C}(2\omega)$ are the amplitudes of x and y components of linear and second harmonic modes. The input linear response function is defined as $\chi_{\text{in}+} = |u^{y,(1)}_{1C}(\omega)|/F^{\text{ext}}$, and the output linear transmission susceptibility is defined as $\chi^{(1)}_{\text{out}+} = |u^{y,(1)}_{N_2C}(\omega)|/F^{\text{ext}}$. The output second harmonic transmission susceptibility is calculated through $\chi^{(2)}_{\text{out}+} = |\vec{u}^{(2)}_{N_2C}(2\omega)|/F^{\text{ext}}$.

All aforementioned numerical parameters, such as N_1, N_2, m, K, η, l_0, $\vec{F}^{\text{ext}}$, and ω, are carried over to the simulations of the nontopological kagome lattice, and the topological lattice with on-site pinning potentials. Here the on-site pinning strength is $K' = K/100 = 1/100$. In the simulation of the topological kagome lattice with on-site pinnings, we further illustrate the input response displacement in Fig. 3(f) and the second harmonic transmission displacement in Fig. 3(g) when the harmonic driving is replaced by Gaussian tone burst $F^{\text{ext}}(t) \sim F^{\text{ext}}e^{i\omega t-(t-t_0)^2/\tau^2}$ with the amplitude $F^{\text{ext}} = 10^{-4}$, the carrier frequency $\omega = 0.06$, and the spread parameter $\tau = 10\pi/\omega$. By varying the carrier frequency from $\omega = 0.0055$ to $\omega = 0.1210$ (and by varying $\tau = 10\pi/\omega$ accordingly), we plot the input linear response function in Fig. 3(h) and the output linear and second harmonic transmission susceptibility curves in Fig. 3(i) to verify linear reciprocity as well as second harmonic nonreciprocal transmission against the Gaussian tone burst.

APPENDIX E: ENERGY TRANSMISSION EFFICIENCY OF PHONON DIODES

An important feature of acoustic diodes which quantitatively characterizes their functionality is the energy transmission efficiency. There has been considerable discussion on the efficiencies of phononic diodes and efforts to improve them, such as Refs. [47,62]. Here we discuss this quantity of our phonon diodes in detail.

In Ref. [47], Liu *et al.* proposed a nonreciprocal acoustic device which transmits *linear* elastic waves with very high energy transmission efficiency $R_+ \approx 1$ and $R_- \approx 0$, where $R_+ = \dot{E}_{\text{out}+}/\dot{E}_{\text{in}+}$ ($R_- = \dot{E}_{\text{out}-}/\dot{E}_{\text{in}-}$) is the power-transmission rate of the phonon diode in the positive (negative) direction defined as the ratio between the output and input wave power. By leveraging the unified techniques of asymmetric incident wave magnification and amplitude-dependent dispersion $\omega = \omega(A)$, their scheme transmits linear waves in one direction by allowing the frequency to fall into the passband, while it blocks the sound in the opposite since the frequency falls into the band gap. The energy transmission efficiency is extremely high since the linear modes carry most of the acoustic energy.

In Ref. [62], Fu *et al.* offer a different nonreciprocal metamaterial consisting of an asymmetric frequency converter and linear wave filter. In contrast to Ref. [47], their device transmits *nonlinear* waves, which is a closer idea to our work. However, unlike our scheme which transmits second harmonic waves, the nonreciprocal transmission of Ref. [62] stems from subharmonic waves which carry the most significant amount of energy, with very high primary transmission efficiency $R_+ \sim 61\%$ and a wide working bandwidth.

While our results take advantage of the novel topological protection and boundary floppy modes in *uniform* metamaterials, the energy transmission efficiency is pretty low compared to Refs. [47,62]. To demonstrate this, we estimate the highest energy transmission rates $R_+ = 4(\chi^{(2)}_{\mathrm{out}+}/\chi_{\mathrm{in}+})^2$ and $R_- = 4(\chi^{(2)}_{\mathrm{out}-}/\chi_{\mathrm{in}-})^2$ in the 1D topological chain [data depicted in Figs. 1(c) and 1(d)] and in a 2D topological lattice with on-site pinnings [data from Figs. 3(c) and 3(d)]. The highest energy transmission rates in 1D and 2D topological lattices are $\max[(R_+, R_-)_{\mathrm{1D\,lattice}}] \sim (2 \times 10^{-10}, 10^{-13})$ and $\max[(R_+, R_-)_{\mathrm{2D\,kagome}}] \sim (10^{-5}, 4 \times 10^{-10})$, respectively. At first glance, one may argue that two ways can largely improve the energy transmission efficiency of our work. First, we could try increasing the shaking force amplitude F^{ext} by orders of magnitude, and the second harmonic transmission susceptibilities $\chi^{(2)}_{\mathrm{out}\pm}$ should increase together. However, this proposal is disproved because chaos naturally arises for huge nonlinearities, especially the lattice boundary on which topological floppy modes are localized. In fact, the driving force amplitude $F^{\mathrm{ext}} = 10^{-4}$ is already as far as we could to have nonlinear modes without exciting chaos. The second way to improve energy transmission is to construct smaller lattices. The unit cell numbers $N_{\mathrm{1D\,lattice}} = 50$ and $N_{\mathrm{2D\,kagome}} = 40$ adopted in our simulations are too large compared to $N = 16$ in Ref. [47] and $N = 7$ in Ref. [62]. Smaller lattices can indeed largely improve the transmission efficiency, but is still not as high as $R_+ \sim O(1)$. Second harmonic modes do not carry the majority of elastic energy, in sharp contrast to linear and subharmonic waves. In conclusion, our results simply present a possible design of the interplay between topological protection and unidirection transport, rather than the optimized version of acoustic diodes. It is therefore interesting to ask whether the combined techniques of topological protection and optimized acoustic diodes can be realized in future research.

[1] R. Süsstrunk and S. D. Huber, Science **349**, 47 (2015).
[2] C. Kane and T. Lubensky, Nat. Phys. **10**, 39 (2014).
[3] R. K. Pal, M. Schaeffer, and M. Ruzzene, J. Appl. Phys. **119**, 084305 (2016).
[4] S. H. Mousavi, A. B. Khanikaev, and Z. Wang, Nat. Commun. **6**, 8682 (2015).
[5] E. Prodan and C. Prodan, Phys. Rev. Lett. **103**, 248101 (2009).
[6] L. M. Nash, D. Kleckner, A. Read, V. Vitelli, A. M. Turner, and W. T. Irvine, Proc. Natl. Acad. Sci. USA **112**, 14495 (2015).
[7] N. P. Mitchell, L. M. Nash, D. Hexner, A. M. Turner, and W. T. Irvine, Nat. Phys. **14**, 380 (2018).
[8] N. P. Mitchell, L. M. Nash, and W. T. M. Irvine, Phys. Rev. B **98**, 174301 (2018).
[9] Z. Zhang, Y. Tian, Y. Cheng, X. Liu, and J. Christensen, Phys. Rev. B **96**, 241306(R) (2017).
[10] H. Dai, J. Jiao, B. Xia, T. Liu, S. Zheng, and D. Yu, J. Phys. D: Appl. Phys. **51**, 175302 (2018).
[11] Y. Guo, T. Dekorsy, and M. Hettich, Sci. Rep. **7**, 18043 (2017).
[12] Z. Yang, F. Gao, X. Shi, X. Lin, Z. Gao, Y. Chong, and B. Zhang, Phys. Rev. Lett. **114**, 114301 (2015).
[13] D. Z. Rocklin, S. Zhou, K. Sun, and X. Mao, Nat. Commun. **8**, 14201 (2017).
[14] L. Zhang and X. Mao, New J. Phys. **20**, 063034 (2018).
[15] J. Paulose, A. S. Meeussen, and V. Vitelli, Proc. Natl. Acad. Sci. USA **112**, 7639 (2015).
[16] H. Abbaszadeh, A. Souslov, J. Paulose, H. Schomerus, and V. Vitelli, Phys. Rev. Lett. **119**, 195502 (2017).
[17] D. Zhou, L. Zhang, and X. Mao, Phys. Rev. Lett. **120**, 068003 (2018).
[18] D. Zhou, L. Zhang, and X. Mao, Phys. Rev. X **9**, 021054 (2019).
[19] A. S. Meeussen, J. Paulose, and V. Vitelli, Phys. Rev. X **6**, 041029 (2016).
[20] J. Paulose, B. G.-g. Chen, and V. Vitelli, Nat. Phys. **11**, 153 (2015).
[21] A. Maznev, A. Every, and O. Wright, Wave Motion **50**, 776 (2013).
[22] J. C. Maxwell, Philos. Mag. J. sci **27**, 294 (1864).
[23] E. Betti, Il Nuovo Cimento (1869-1876) **7**, 158 (1872).
[24] T. Charlton, Nature (London) **187**, 231 (1960).
[25] P. Wang, L. Lu, and K. Bertoldi, Phys. Rev. Lett. **115**, 104302 (2015).
[26] N. P. Mitchell, L. M. Nash, and W. T. M. Irvine, Phys. Rev. B **97**, 100302(R) (2018).
[27] N. Engheta, A. Salandrino, and A. Alù, Phys. Rev. Lett. **95**, 095504 (2005).
[28] A. Souslov, K. Dasbiswas, M. Fruchart, S. Vaikuntanathan, and V. Vitelli, Phys. Rev. Lett. **122**, 128001 (2019).
[29] Y. Wang, B. Yousefzadeh, H. Chen, H. Nassar, G. Huang, and C. Daraio, Phys. Rev. Lett. **121**, 194301 (2018).
[30] M. B. Zanjani, A. R. Davoyan, A. M. Mahmoud, N. Engheta, and J. R. Lukes, Appl. Phys. Lett. **104**, 081905 (2014).
[31] G. Trainiti and M. Ruzzene, New J. Phys. **18**, 083047 (2016).
[32] H. Nassar, X. Xu, A. Norris, and G. Huang, J. Mech. Phys. Solids **101**, 10 (2017).
[33] N. Swinteck, S. Matsuo, K. Runge, J. Vasseur, P. Lucas, and P. A. Deymier, J. Appl. Phys. **118**, 063103 (2015).
[34] R. Fleury, A. B. Khanikaev, and A. Alu, Nat. Commun. **7**, 11744 (2016).
[35] G. Salerno, T. Ozawa, H. M. Price, and I. Carusotto, Phys. Rev. B **93**, 085105 (2016).

[36] R. Chaunsali, F. Li, and J. Yang, Sci. Rep. **6**, 30662 (2016).

[37] V. Peano, C. Brendel, M. Schmidt, and F. Marquardt, Phys. Rev. X **5**, 031011 (2015).

[38] R. Fleury, D. L. Sounas, C. F. Sieck, M. R. Haberman, and A. Alù, Science **343**, 516 (2014).

[39] A. Souslov, B. C. Van Zuiden, D. Bartolo, and V. Vitelli, Nat. Phys. **13**, 1091 (2017).

[40] T. Devaux, V. Tournat, O. Richoux, and V. Pagneux, Phys. Rev. Lett. **115**, 234301 (2015).

[41] A. Merkel, V. Tournat, and V. Gusev, Phys. Rev. E **90**, 023206 (2014).

[42] A. Cebrecos, N. Jiménez, V. Romero-García, R. Picó, V. J. Sánchez-Morcillo, and L. García-Raffi, AIP Adv. **6**, 121601 (2016).

[43] N. Nadkarni, A. F. Arrieta, C. Chong, D. M. Kochmann, and C. Daraio, Phys. Rev. Lett. **116**, 244501 (2016).

[44] C. Coulais, D. Sounas, and A. Alù, Nature (London) **542**, 461 (2017).

[45] N. Boechler, G. Theocharis, and C. Daraio, Nat. Mater. **10**, 665 (2011).

[46] B. Liang, X. Guo, J. Tu, D. Zhang, and J. Cheng, Nat. Mater. **9**, 989 (2010).

[47] C. Liu, Z. Du, Z. Sun, H. Gao, and X. Guo, Phys. Rev. Appl. **3**, 064014 (2015).

[48] Z.-m. Gu, J. Hu, B. Liang, X.-y. Zou, and J.-c. Cheng, Sci. Rep. **6**, 19824 (2016).

[49] D. Z. Rocklin, B. G.-g. Chen, M. Falk, V. Vitelli, and T. C. Lubensky, Phys. Rev. Lett. **116**, 135503 (2016).

[50] T. Lubensky, C. Kane, X. Mao, A. Souslov, and K. Sun, Rep. Prog. Phys. **78**, 073901 (2015).

[51] J. Ma, D. Zhou, K. Sun, X. Mao, and S. Gonella, Phys. Rev. Lett. **121**, 094301 (2018).

[52] M. Deng, P. Wang, and X. Lv, J. Phys. D: Appl. Phys. **38**, 344 (2005).

[53] K. H. Matlack, J.-Y. Kim, L. J. Jacobs, and J. Qu, J. Appl. Phys. **109**, 014905 (2011).

[54] R. Ganesh and S. Gonella, Phys. Rev. Lett. **114**, 054302 (2015).

[55] R. Ganesh and S. Gonella, J. Mech. Phys. Solids **99**, 272 (2017).

[56] W. Jiao and S. Gonella, Phys. Rev. E **99**, 042206 (2019).

[57] R. K. Pal, J. Vila, M. Leamy, and M. Ruzzene, Phys. Rev. E **97**, 032209 (2018).

[58] W. Jiao and S. Gonella, J. Mech. Phys. Solids **111**, 1 (2018).

[59] W. Jiao and S. Gonella, Phys. Rev. Appl. **10**, 024006 (2018).

[60] B. G.-g. Chen, N. Upadhyaya, and V. Vitelli, Proc. Natl. Acad. Sci. USA **111**, 13004 (2014).

[61] S. Guest and J. Hutchinson, J. Mech. Phys. Solids **51**, 383 (2003).

[62] C. Fu, B. Wang, T. Zhao, and C. Chen, Appl. Phys. Lett. **112**, 051902 (2018).